

XQR-30: Black hole masses and accretion rates of 42 $z \gtrsim 6$ quasars

C. Mazzucchelli¹, M. Bischetti², V. D’Odorico^{2,3,4}, C. Feruglio², J.-T. Schindler⁵, M. Onoue^{6,7}, E. Bañados⁸, G. D. Becker⁹, F. Bian¹⁰, S. Carniani³, R. Decarli¹¹, A.-C. Eilers^{12,*}, E. P. Farina¹³, S. Gallerani³, S. Lai¹⁴, R. A. Meyer⁸, S. Rojas-Ruiz⁸, S. Satyavolu¹⁵, B. P. Venemans⁵, F. Wang¹⁶, J. Yang¹⁶, and Y. Zhu⁹

¹ Instituto de Estudios Astrofísicos, Facultad de Ingeniería y Ciencias, Universidad Diego Portales, Avenida Ejército Libertador 441, Santiago, Chile
e-mail: chiara.mazzucchelli@mail.udp.cl

² INAF – Osservatorio Astronomico di Trieste, Via G.B. Tiepolo, 11, 34143 Trieste, Italy

³ Scuola Normale Superiore, P.zza dei Cavalieri 7, 56126 Pisa, Italy

⁴ IFPU – Institute for Fundamental Physics of the Universe, Via Beirut 2, 34151 Trieste, Italy

⁵ Leiden Observatory, Leiden University, Niels Bohrweg 2, 2333 CA Leiden, The Netherlands

⁶ Kavli Institute for Astronomy and Astrophysics, Peking University, Beijing 100871, PR China

⁷ Kavli Institute for the Physics and Mathematics of the Universe (Kavli IPMU, WPI), The University of Tokyo, Chiba 277-8583, Japan

⁸ Max Planck Institut für Astronomie, Königstuhl 17, 69117 Heidelberg, Germany

⁹ Department of Physics & Astronomy, University of California, Riverside, CA 92521, USA

¹⁰ ESO, Vitacura Alonso de Córdova 3107, Vitacura, Casilla 19001, Santiago de Chile, Chile

¹¹ INAF – Osservatorio di Astrofisica e Scienza dello Spazio di Bologna, Via Gobetti 93/3, 40129 Bologna, Italy

¹² MIT Kavli Institute for Astrophysics and Space Research, 77 Massachusetts Avenue, Cambridge, MA 02139, USA

¹³ Gemini Observatory, NSF’s NOIRLab, 670 N A’ohoku Place, Hilo, HI 96720, USA

¹⁴ Research School of Astronomy and Astrophysics, Australian National University, Canberra, ACT 2611, Australia

¹⁵ Tata Institute of Fundamental Research, Homi Bhabha Road, Mumbai 400005, India

¹⁶ Steward Observatory, University of Arizona, 933 N Cherry Avenue, Tucson, AZ 85721, USA

Received 3 March 2023 / Accepted 17 June 2023

ABSTRACT

We present bolometric luminosities, black hole masses, and Eddington ratios for 42 luminous quasars at $z \gtrsim 6$ using high signal-to-noise ratio VLT/X-shooter spectra, acquired as part of the enlarged ESO Large Programme *XQR-30*. In particular, we derived the bolometric luminosities from the rest-frame 3000 Å luminosities using a bolometric correction from the literature, as well as the black hole masses by modeling the spectral regions around the C IV 1549 Å and the Mg II 2798 Å emission lines, with scaling relations calibrated in the Local Universe. We find that the black hole masses derived from both emission lines are in the same range and the scatter of the measurements agrees with expectations from the scaling relations. The Mg II-derived masses are between $\sim(0.8-12) \times 10^9 M_{\odot}$ and the derived Eddington ratios are within $\sim 0.13-1.73$, with a mean (median) of 0.84(0.72). By comparing the total sample of quasars at $z > 5.8$, from this work and from the literature, to a bolometric luminosity distribution-matched sample at $z \sim 1.5$, we find that quasars at high redshift host slightly less massive black holes, which accrete slightly more rapidly than those at lower z , with a difference in the mean Eddington ratios of the two samples of ~ 0.27 . These findings are in agreement with the results of recent works in the literature.

Key words. quasars: supermassive black holes – quasars: emission lines – galaxies: high-redshift

1. Introduction

Quasars are the most luminous, non-transient sources in the universe, hence, they can be observed at very early Cosmic times, into the Epoch of Reionization at $z \gtrsim 6$ (within the first billion years of the universe; e.g., Jiang et al. 2015, 2016; Bañados et al. 2016; Reed et al. 2019; Matsuoka et al. 2019) up to $z \sim 7.5$ (e.g., Bañados et al. 2018; Yang et al. 2020; Wang et al. 2021; see Fan et al. 2022 for a recent review). They are already powered by supermassive black holes (SMBHs) in their centers ($M_{\text{BH}} > 10^8 M_{\odot}$ e.g., Jiang et al. 2007; Shen et al. 2019), challenging models of early black hole formation and growth (e.g., Inayoshi et al. 2020; Volonteri et al. 2021 for recent reviews),

and already present evolved broad line regions (BLRs) with super-solar metallicities (e.g., Kurk et al. 2007; Lai et al. 2022). In order to grow a billion-solar masses SMBH by $z \gtrsim 6$, models require either a “light” ($\sim 10^2 M_{\odot}$) SMBH seed undergoing rapid super-Eddington accretion episodes or a “heavy” ($\sim 10^5 M_{\odot}$) seed, which could also grow sub-Eddington (e.g., Volonteri 2010). Current studies identify PopIII stars as main candidates of the progenitors of light seeds (e.g., Bond et al. 1984; Valiante et al. 2016), while direct collapse of large primordial, low-metallicity gas clouds produce $\sim 10^{5-6} M_{\odot}$ seeds (e.g., Oh & Haiman 2002; Begelman et al. 2006; Ferrara et al. 2014). Alternatively, runaway collisions and stellar-dynamical interactions in dense primordial star clusters can form seeds with intermediate masses ($\sim 10^{3-4} M_{\odot}$; e.g., Devecchi & Volonteri 2009; Sakurai et al. 2017). Another possibility for growing the

* Pappalardo Fellow.

observed black hole masses is a radiatively inefficient accretion scenario, which may allow for $100\times$ higher mass accretion rates while remaining sub-Eddington, although this would require a large fraction of obscured quasars at high- z (e.g., [Davies et al. 2019](#)). Constraints from observational studies of black hole masses and accretion rates of sources at $z \gtrsim 6$ are therefore fundamental to inform SMBH formation theories and models as well as to position them in the context of their (co-)evolution with their host galaxies (e.g., [Pensabene et al. 2020](#); [Neeleman et al. 2021](#)).

Currently, ~ 100 measurements of $z \gtrsim 5.8$ SMBH masses have been reported in the literature, from ground-based near-infrared (NIR) spectroscopic data with limited signal-to-noise ratios (S/Ns; e.g., [Shen et al. 2019](#); [Yang et al. 2021](#); see [Fan et al. 2022](#) for a recent review). The backbone of such studies is the modeling of the region around the rest-frame UV Mg II 2798 Å emission line, which can be used to derive black hole masses and accretion rates once virial equilibrium is assumed and while taking advantage of scaling relations calibrated in the local universe (e.g., [Vestergaard & Osmer 2009](#)). Another routinely used emission line for measuring black hole masses is the C IV 1549 Å (e.g., [Vestergaard & Peterson 2006](#)), especially in cases in which the Mg II falls in or close to telluric absorption, even when it is necessary to consider larger uncertainties due to intrinsic, non-virial components of the C IV line, arising from winds or outflows (e.g., [Coatman et al. 2017](#)). Although some studies suggest that $z \gtrsim 6$ quasars accrete at a rate that is comparable to that of a luminosity distribution-matched sample of quasars at $z \sim 1-2$ (e.g., [Mazzucchelli et al. 2017](#); [Shen et al. 2019](#)), others have observed a slight increase in the Eddington ratio as a function of redshift (e.g., [Yang et al. 2021](#); [Farina et al. 2022](#)). One of the main drawbacks of literature work so far is the low S/N of the considered data, which may introduce biases in the properties derived by the spectral fitting (e.g., [Denney et al. 2016](#)) and could highly deteriorate the C IV or Mg II line modeling in the case of strong absorption features.

In this paper, we present measurements of bolometric luminosities, black hole masses, and accretion rates from the modeling of the Mg II and C IV emission line regions for a sample of 42 luminous $z \sim 6$ quasars from the enlarged XQR-30 survey (E-XQR-30). In particular, 30 objects were observed in the Legacy Survey of quasars at $z = 5.8-6.6$ XQR-30 ([D’Odorico et al. 2023](#); also referred to as the “XQR30 Core” here) and 12 sources with similar properties and available X-Shooter observations with comparable S/Ns were obtained from the literature (also referred to as “XQR30 Extended” here). This is the first sample with such a high S/N ($\gtrsim 11-114$ per bin of 10 km s^{-1} ; [D’Odorico et al. 2023](#)) optical/NIR spectra, which allows us to carry out an accurate modeling of their emission lines. Out of the total sample, black hole masses and accretion rates for 19 objects are reported for the first time.

This work is organized as follows. In Sect. 2, we describe the sample and we briefly report the data reduction. In Sect. 3, we report the spectral modeling. In Sect. 4, we present our measurements and we compare the black hole masses obtained via C IV and Mg II emission line modeling. We place our work in the context of quasars at lower redshift and we compare them with current measurements of high- z quasars properties from the literature. We list our conclusions and outlook for future studies in Sect. 5. Throughout the paper, magnitudes are reported in the AB system and we use a flat cosmology with $H_0 = 70 \text{ km s}^{-1} \text{ Mpc}^{-1}$, $\Omega_M = 0.3$, and $\Omega_\Lambda = 0.7$.

2. Sample and data reduction

XQR-30 is an ESO Large Program (Program ID: 1103.A-0817(A); PI: D’Odorico) with high S/N ($\sim 11-41$ in the continuum at rest-frame wavelength of 1285 Å) spectra for 30 high- z quasars observed with the X-shooter spectrograph ([Vernet et al. 2011](#)) at the VLT ([D’Odorico et al. 2023](#)). The quasars were selected to be observable from Paranal Observatory (Decl. < 27 deg), with redshift in the range of $5.8 \lesssim z \lesssim 6.6$, and AB magnitude of $J \lesssim 19.8(20.0)$ for $z < 6.0(6.0 \lesssim z \lesssim 6.6)$. This survey is aimed at addressing several goals, from the characterization of the reionization process to the study of absorbers along the line of sight and the early metal enrichment of the quasars’ BLRs and circumgalactic medium (CGM). We also consider 12 additional quasars with analogous luminosities and redshifts, and with X-Shooter spectra with comparable S/Ns ($\sim 17-114$ at a rest-frame of 1285 Å) available in the archive (data previously published in [Becker et al. 2015](#); [Bosman et al. 2018](#); [Schindler et al. 2020](#)). The spectra for the entire sample were treated with a consistent methodology.

In brief, the data were reduced with a custom-made pipeline optimized for faint sources ([López et al. 2016](#); [Becker et al. 2019](#)). After a standard reduction, the correction for telluric absorption was obtained using models created with ESO SKY-CALC Cerro Paranal Advanced Sky Model ([Noll et al. 2012](#); [Jones et al. 2013](#)). The relative flux calibration is measured with a static response function calculated from a standard star. The 1D stacked spectra of the VIS and NIR arms were combined using Astrocook ([Cupani et al. 2018, 2020](#)) and re-binned to a constant velocity step of 50 km s^{-1} . Each quasar’s spectrum was absolute-flux calibrated by scaling it to match the observed AB band magnitude in the J band ([D’Odorico et al. 2023](#)). For a full description of the sample and data reduction, we refer to [D’Odorico et al. \(2023\)](#).

3. Modeling of the spectra

Quasars’ rest-frame UV/optical spectra are characterized by a pseudo-continuum, due to different emission processes and broad emission lines. To model these spectra, we followed the approach described in [Mazzucchelli et al. \(2017\)](#) and [Schindler et al. \(2020\)](#). Details of the spectral modeling will be presented in a forthcoming paper ([Bischetti et al., in prep.](#)) and here, we summarize the main spectral components as follows: (i) A power-law quasar continuum emission; in the case of the reddest quasars, we also included a second or third polynomial function to better fit the part of the spectrum blueward of the C IV (e.g., [Shen et al. 2019](#)). To model this pseudo continuum, we consider regions of the spectra free of strong emission line features or of absorption due to the atmosphere (e.g., [Schindler et al. 2020](#)). (ii) A Balmer pseudo continuum (f_{BC}), using the equation from [Dietrich et al. \(2003\):](#)

$$f_{\text{BC}}(\lambda) = f_{\text{BC},0} B_\lambda(\lambda, T_e) \left(1 - e^{-\tau_{\text{BE}}(\lambda/\lambda_{\text{BE}})^3} \right), \quad (1)$$

with values for the electron temperature ($T_e = 15000 \text{ K}$) and optical depth ($\tau_{\text{BE}} = 1$) as used in other works (e.g., [De Rosa et al. 2014](#); [Mazzucchelli et al. 2017](#)). We impose the Balmer emission to 30% of the pseudo-continuum contribution, as above described, at rest-frame 3646 Å (e.g. [Schindler et al. 2020](#); [Farina et al. 2022](#)). The Balmer pseudo-continuum and the power-law function are modelled at the same time. (iii) A Fe II pseudo-continuum, using the empirical template from [Vestergaard & Wilkes \(2001\)](#), which is used to derive the Mg II

emission line-based scaling relation to calculate black hole masses in Sect. 4. The empirical template, shifted using an initial redshift measured from the Mg II emission line, is convolved with a Gaussian convolution kernel of different values depending on each spectrum. (iv) One (or more) Gaussian function(s) is used to model the broad emission lines, with a upper limit to the full width at half maximum ($FWHM$) $< 10\,000\text{ km s}^{-1}$, which prevents the model from using a very broad Gaussian function to model weak Fe II emission not perfectly reproduced by the Vestergaard & Wilkes (2001) template.

Here, in case the emission lines were fit with more than one Gaussian function, we calculated the best values and uncertainties for the properties of the entire line following the method reported in Schindler et al. (2020). Briefly, for each line for which two or three Gaussian functions were used, we create $N = 1000$ replication of each of the best Gaussian fits. For each replication, the mean and standard deviation of each fit are randomly drawn from Gaussian distributions, whose respective mean and standard deviation are fixed to the best fit value and associated uncertainty, respectively. Then, in each replication, we sum the single Gaussian functions and we calculate the total FWHM as the distance between the two wavelengths where the flux is equal to half the maximum. All the 1000 FWHM values so obtained were then distributed as a Gaussian function. We considered the mean and sigma of such a distribution as the best value and uncertainty for the final FWHM of the line. The final $FWHM_{Mg\text{ II}}$ and $FWHM_{C\text{ IV}}$ values are reported in Table 1. In Fig. 1, we show the fit of the spectral region around the Mg II emission line. We note that in few cases, the Mg II emission line falls very close to (PSOJ007+04, PSOJ009–10, PSOJ183–12, PSOJ065+01) or within (PSOJ023–02, PSOJ025–11, PSOJ242–12) a region affected by strong telluric absorption. Therefore, also given the potential degeneracies of our spectral modeling with several components, the fit results and relative derived quantities (e.g., black hole masses, bolometric luminosities, Eddington ratios) should be taken with caution.

4. Data analysis

In this section, we derive the quasars' black hole masses, luminosities, and accretion rates, relying on the fit of both the C IV and Mg II wavelength regions.

4.1. Calculating the black hole masses and Eddington ratios

Mg II. To derive black hole masses, we use the scaling relation provided by Vestergaard & Osmer (2009):

$$M_{\text{BH},\text{Mg II}} = 10^{6.86} \left[\frac{FWHM_{\text{Mg II}}}{10^3 \text{ km s}^{-1}} \right]^2 \left[\frac{\lambda L_{\lambda}(3000 \text{ \AA})}{10^{44} \text{ erg s}^{-1}} \right]^{0.5} M_{\odot}, \quad (2)$$

where $\lambda L_{\lambda}(3000 \text{ \AA})$ is the monochromatic luminosity at rest-frame wavelength 3000 \AA . Systematic uncertainties in SMBH masses are estimated to be ~ 0.55 dex.

C IV. In this case, we use the scaling relation from Vestergaard & Peterson (2006):

$$M_{\text{BH},\text{C IV}} = 10^{6.66} \left[\frac{FWHM_{\text{C IV,corr}}}{10^3 \text{ km s}^{-1}} \right]^2 \left[\frac{\lambda L_{\lambda}(1350 \text{ \AA})}{10^{44} \text{ erg s}^{-1}} \right]^{0.53} M_{\odot}, \quad (3)$$

where the $\lambda L_{\lambda}(1350 \text{ \AA})$ is the monochromatic luminosity at rest-frame wavelength 1350 \AA and $FWHM_{\text{C IV,corr}}$ is the corrected

FWHM of the total C IV emission line. It is important to note that the C IV emission line profile is affected by the presence of an outflowing component (e.g., Richards et al. 2006; Meyer et al. 2019). Therefore, we use the equation from Coatman et al. (2017) to obtain the corrected value of the FWHM:

$$FWHM_{\text{C IV,corr}} = \frac{FWHM_{\text{C IV}}}{0.36 \times \frac{C\text{ IV Blueshift}}{10^3 \text{ km s}^{-1}} + 0.61} \quad (4)$$

where C IV Blueshift is the velocity difference between the C IV centroid and the quasars' systemic redshifts (obtained from the Mg II or from the [C II] emission line, when available, as reported in D'Odorico et al. 2023, and in Table 1), in units of km s^{-1} . In this case, the uncertainties measured on the Vestergaard & Peterson (2006) relation is ~ 0.40 dex, while it is estimated to be reduced to ~ 0.24 dex with the correction by Coatman et al. (2017). We calculated both $L_{\lambda}(1350 \text{ \AA})$ and $L_{\lambda}(3000 \text{ \AA})$ using the value of the fluxes at 1350 \AA and 3000 \AA from the power-law fit.

From the black hole mass measurements, we can calculate the Eddington luminosity as:

$$L_{\text{Edd,C IV/Mg II}} = 1.3 \times 10^{38} \left(\frac{M_{\text{BH,C IV/Mg II}}}{M_{\odot}} \right) \text{ erg s}^{-1}. \quad (5)$$

We also computed the bolometric luminosity (L_{bol}) using the bolometric correction presented by Richards et al. (2006):

$$L_{\text{bol}} = 5.15 \lambda L_{\lambda}(3000 \text{ \AA}) \text{ erg s}^{-1}. \quad (6)$$

We note that it has been discussed that such bolometric correction might be overestimated for highly luminous quasars (e.g., Trakhtenbrot & Netzer 2012). Nevertheless, we decide to use it for consistency with several works in the literature (e.g., Mazzucchelli et al. 2017; Yang et al. 2021; Farina et al. 2022). From the L_{Edd} and L_{bol} values we can derive the corresponding Eddington ratios $\lambda_{\text{Edd,C IV}} = L_{\text{bol}}/L_{\text{Edd,C IV}}$ and $\lambda_{\text{Edd,Mg II}} = L_{\text{bol}}/L_{\text{Edd,Mg II}}$. We report the values of the monochromatic and bolometric luminosities, black hole masses and Eddington ratios in Table 1.

4.2. C IV vs. Mg II black hole masses comparison

We compare the black hole masses measured from modeling of the C IV and Mg II emission line region in Fig. 2. The two measurements are approximately in the same range, although the C IV based values are slightly higher than the Mg II ones, with a mean ratio of $M_{\text{BH,C IV}}/M_{\text{BH,Mg II}} \sim 1.3$. On the other hand, as discussed in Farina et al. (2022), we also notice that the C IV modeling tends to underestimate the values of black hole masses for higher $M_{\text{BH,Mg II}}$ values, namely, for higher $FWHM_{\text{Mg II}}$ values. Finally, we also notice that a high fraction of broad-absorption-line (BAL) quasars have been recovered in the XQR-30 sample ($\sim 50\%$; Bischetti et al. 2022). Even though BAL features may complicate the fit of the C IV emission line region, the high S/N of our spectra still permits a good modeling of the line in the majority of the cases. The quasar PSO J065+01 stands out as a particular outlier, with a C IV-based mass lower than that recovered from the Mg II line by a factor of ~ 1.3 dex. This is due to the very peculiar shape of the quasar spectrum, and the very low S/N of the C IV emission line.

If one considers the Mg II line-derived BH masses as the reference values, we can estimate the mean (median) of the dispersion of the C IV line-derived values to be $0.28(0.21)$ dex. If

Table 1. Enlarged XQR-30 Sample: Redshift derived from the Mg II emission line modeling or, when available, from the [C II] emission line (see D’Odorico et al. 2023); C IV and Mg II full-width at half maximum; C IV blueshift (used in Eq. (4)); monochromatic luminosities at rest-frame 1350 Å and 3000 Å; bolometric luminosities; black hole masses and Eddington ratio values, derived from both the C IV and Mg II emission lines.

| Name | Redshift | $FWHM_{C\,IV}$ [km s ⁻¹] | $FWHM_{Mg\,II}$ [km s ⁻¹] | C IV Blueshift [km s ⁻¹] | $\log \lambda L_{1350}$ [erg s ⁻¹] | $\log \lambda L_{3000}$ [erg s ⁻¹] | $\log L_{bol}$ [erg s ⁻¹] | $\log M_{BH,C\,IV}$ [M _⊙] | $\log M_{BH,Mg\,II}$ [M _⊙] | $\lambda_{Edd,C\,IV}$ | $\lambda_{Edd,Mg\,II}$ |
|--------------------------------|-----------------------|---|--|---|---|---|--|--|---|-----------------------|------------------------|
| PSOJ007+04 ^(a) | 6.0015 ^(†) | 6169±1057 | 8176±473 | 2778±601 | 46.56 ^{+0.05} _{-0.06} | 46.41 ^{+0.15} _{-0.22} | 47.12 ^{+0.15} _{-0.22} | 9.16 ^{+0.19} _{-0.35} | 9.89 ^{+0.09} _{-0.11} | 0.71±0.49 | 0.13±0.06 |
| PSOJ009-10 ^(‡,a) | 6.004 ^(†) | 8025±2963 | 7336±697 | 2956±456 | 46.42 ^{+0.06} _{-0.06} | 46.63 ^{+0.08} _{-0.09} | 47.34 ^{+0.08} _{-0.09} | 9.28 ^{+0.26} _{-0.71} | 9.9 ^{+0.08} _{-0.1} | 0.88±0.73 | 0.21±0.06 |
| PSOJ023-02 ^(‡,a) | 5.90 | 4806±486 | 4065±201 | 832±112 | 46.39 ^{+0.04} _{-0.04} | 46.62 ^{+0.06} _{-0.07} | 47.33 ^{+0.06} _{-0.07} | 9.37 ^{+0.13} _{-0.18} | 9.39 ^{+0.05} _{-0.06} | 0.7±0.26 | 0.68±0.12 |
| PSOJ025-11 ^(a) | 5.85 | 5283±1043 | 3976±196 | 1316±286 | 46.68 ^{+0.03} _{-0.04} | 46.56 ^{+0.09} _{-0.11} | 47.27 ^{+0.09} _{-0.11} | 9.45 ^{+0.2} _{-0.39} | 9.34 ^{+0.06} _{-0.07} | 0.51±0.32 | 0.66±0.18 |
| PSOJ029-29 | 5.984 | 6886±1190 | 3501±292 | 2063±285 | 46.88 ^{+0.02} _{-0.03} | 46.78 ^{+0.07} _{-0.08} | 47.49 ^{+0.07} _{-0.08} | 9.58 ^{+0.16} _{-0.25} | 9.34 ^{+0.07} _{-0.09} | 0.63±0.3 | 1.1±0.27 |
| ATLASJ029-36 | 6.02 | 5808±1517 | 3753±266 | 1924±377 | 46.73 ^{+0.01} _{-0.01} | 46.38 ^{+0.03} _{-0.03} | 47.1 ^{+0.03} _{-0.03} | 9.39 ^{+0.22} _{-0.07} | 9.2 ^{+0.06} _{-0.06} | 0.4±0.26 | 0.6±0.1 |
| VDESJ0224-4711 | 6.526 | 5378±207 | 2863±206 | 1808±42 | 46.61 ^{+0.04} _{-0.05} | 46.82 ^{+0.06} _{-0.06} | 47.54 ^{+0.06} _{-0.06} | 9.29 ^{+0.04} _{-0.05} | 9.19 ^{+0.06} _{-0.08} | 1.36±0.23 | 1.72±0.36 |
| PSOJ060+24 | 6.18 | 4522±625 | 3270±249 | 633±323 | 46.58 ^{+0.04} _{-0.04} | 46.59 ^{+0.08} _{-0.1} | 47.3 ^{+0.08} _{-0.1} | 9.5 ^{+0.31} _{-0.31} | 9.18 ^{+0.07} _{-0.09} | 0.48±0.52 | 1.01±0.27 |
| J0408-5632 ^(‡) | 6.0345 | 6943±355 | 4057±323 | 2411±155 | 46.55 ^{+0.03} _{-0.04} | 46.48 ^{+0.08} _{-0.1} | 47.19 ^{+0.08} _{-0.1} | 9.33 ^{+0.07} _{-0.08} | 9.31 ^{+0.08} _{-0.09} | 0.55±0.15 | 0.57±0.16 |
| PSOJ065-26 | 6.1871 ^(†) | 8866±2638 | 4878±836 | 3895±1503 | 46.83 ^{+0.01} _{-0.01} | 46.64 ^{+0.04} _{-0.04} | 47.35 ^{+0.04} _{-0.04} | 9.41 ^{+0.3} _{-1.6} | 9.56 ^{+0.13} _{-0.18} | 0.67±0.66 | 0.48±0.17 |
| PSOJ065+01 ^(‡,a,b) | 5.79 | 2389±878 | 5569±849 | 2682±368 | 46.4 ^{+0.05} _{-0.05} | 46.49 ^{+0.08} _{-0.1} | 47.2 ^{+0.08} _{-0.1} | 8.27 ^{+0.25} _{-0.67} | 9.6 ^{+0.12} _{-0.17} | 6.63±5.37 | 0.31±0.12 |
| PSOJ089-15 ^(‡) | 5.957 | 3345±707 | 4365±425 | 1385±164 | 46.6 ^{+0.04} _{-0.05} | 46.86 ^{+0.05} _{-0.06} | 47.57 ^{+0.05} _{-0.06} | 8.99 ^{+0.17} _{-0.29} | 9.57 ^{+0.08} _{-0.1} | 2.94±1.48 | 0.77±0.18 |
| PSOJ108+08 | 5.9485 | 8164±628 | 4247±346 | 3109±281 | 46.84 ^{+0.04} _{-0.04} | 46.75 ^{+0.1} _{-0.13} | 47.46 ^{+0.1} _{-0.13} | 9.48 ^{+0.09} _{-0.12} | 9.49 ^{+0.08} _{-0.1} | 0.74±0.26 | 0.72±0.24 |
| SDSSJ0842+1218 ^(‡) | 6.0754 ^(†) | 6041±270 | 3854±337 | 2078±37 | 46.58 ^{+0.02} _{-0.02} | 46.54 ^{+0.05} _{-0.05} | 47.25 ^{+0.05} _{-0.05} | 9.3 ^{+0.04} _{-0.05} | 9.3 ^{+0.07} _{-0.09} | 0.68±0.11 | 0.68±0.15 |
| J0923+0402 ^(‡) | 6.633 ^(†) | 5940±327 | 3793±799 | 2682±135 | 46.5 ^{+0.06} _{-0.07} | 46.79 ^{+0.07} _{-0.08} | 47.51 ^{+0.07} _{-0.08} | 9.11 ^{+0.07} _{-0.08} | 9.42 ^{+0.16} _{-0.24} | 1.92±0.45 | 0.95±0.44 |
| PSOJ158-14 | 6.0685 ^(†) | 6323±1538 | 3258±212 | 1767±1138 | 46.77 ^{+0.06} _{-0.06} | 46.85 ^{+0.1} _{-0.13} | 47.56 ^{+0.1} _{-0.13} | 9.52 ^{+0.38} _{-0.38} | 9.31 ^{+0.07} _{-0.09} | 0.85±1.19 | 1.37±0.42 |
| PSOJ183+05 | 6.4386 ^(†) | 7075±2010 | 4476±1282 | 3035±348 | 46.69 ^{+0.05} _{-0.06} | 46.49 ^{+0.16} _{-0.25} | 47.2 ^{+0.16} _{-0.25} | 9.29 ^{+0.21} _{-0.42} | 9.41 ^{+0.21} _{-0.41} | 0.62±0.47 | 0.48±0.36 |
| PSOJ183-12 ^(‡,a) | 5.86 | 6196±517 | 3203±517 | 3031±194 | 46.81 ^{+0.02} _{-0.02} | 46.7 ^{+0.06} _{-0.07} | 47.41 ^{+0.06} _{-0.07} | 9.24 ^{+0.08} _{-0.1} | 9.22 ^{+0.12} _{-0.17} | 1.13±0.29 | 1.19±0.43 |
| PSOJ217-16 | 6.1498 ^(†) | 10292±909 | 2772±741 | 3243±1394 | 46.6 ^{+0.04} _{-0.04} | 46.55 ^{+0.08} _{-0.1} | 47.26 ^{+0.08} _{-0.1} | 9.54 ^{+0.27} _{-0.92} | 9.02 ^{+0.19} _{-0.34} | 0.41±0.37 | 1.34±0.79 |
| PSOJ217-07 ^(‡) | 6.1663 | 9174±2402 | 2607±533 | 3260±2169 | 46.46 ^{+0.07} _{-0.08} | 46.42 ^{+0.15} _{-0.23} | 47.13 ^{+0.15} _{-0.23} | 9.35 ^{+0.39} _{-0.39} | 8 ^{+0.16} _{-0.27} | 0.46±0.69 | 1.3±0.8 |
| PSOJ231-20 ^(‡) | 6.5869 ^(†) | 6470±241 | 4644±179 | 2528±116 | 46.74 ^{+0.01} _{-0.01} | 46.65 ^{+0.04} _{-0.04} | 47.36 ^{+0.04} _{-0.04} | 9.34 ^{+0.05} _{-0.06} | 9.52 ^{+0.04} _{-0.04} | 0.79±0.12 | 0.53±0.07 |
| J1535+1943 | 6.370 ^(†) | 6268±654 | 5640±236 | 2353±271 | 46.51 ^{+0.11} _{-0.15} | 46.88 ^{+0.1} _{-0.13} | 47.6 ^{+0.1} _{-0.13} | 9.23 ^{+0.13} _{-0.18} | 9.8 ^{+0.06} _{-0.07} | 1.78±0.77 | 0.48±0.15 |
| PSOJ239-07 ^(‡) | 6.1102 ^(†) | 4863±185 | 3947±79 | 537±63 | 46.72 ^{+0.05} _{-0.06} | 46.74 ^{+0.1} _{-0.13} | 47.46 ^{+0.1} _{-0.13} | 9.68 ^{+0.1} _{-0.13} | 9.42 ^{+0.05} _{-0.06} | 0.46±0.17 | 0.83±0.24 |
| PSOJ242-12 ^(a) | 5.830 | 6791±1672 | 4892±495 | 1152±439 | 46.48 ^{+0.07} _{-0.08} | 46.55 ^{+0.12} _{-0.17} | 47.26 ^{+0.12} _{-0.17} | 9.61 ^{+0.28} _{-1.05} | 9.51 ^{+0.1} _{-0.13} | 0.34±0.33 | 0.43±0.18 |
| PSOJ308-27 | 5.7985 | 5284±148 | 2852±131 | 535±115 | 46.7 ^{+0.02} _{-0.02} | 46.64 ^{+0.06} _{-0.07} | 47.35 ^{+0.06} _{-0.07} | 9.74 ^{+0.16} _{-0.25} | 9.09 ^{+0.05} _{-0.05} | 0.32±0.14 | 1.4±0.26 |
| PSOJ323+12 | 6.5872 ^(†) | 2828±140 | 2450±284 | 326±27 | 46.65 ^{+0.02} _{-0.02} | 46.56 ^{+0.06} _{-0.07} | 47.27 ^{+0.06} _{-0.07} | 9.26 ^{+0.08} _{-0.09} | 8.92 ^{+0.09} _{-0.12} | 0.78±0.19 | 1.73±0.5 |
| VIK J2211-3206 ^(‡) | 6.3394 ^(†) | 5114±224 | 3448±729 | 1811±97 | 46.66 ^{+0.02} _{-0.02} | 46.73 ^{+0.05} _{-0.05} | 47.44 ^{+0.04} _{-0.05} | 9.27 ^{+0.06} _{-0.07} | 9.3 ^{+0.15} _{-0.24} | 1.15±0.2 | 1.06±0.47 |
| VDES J2250-5051 ^(‡) | 5.9767 | 16618±11883 | 5212±4022 | 3001±9685 | 46.58 ^{+0.04} _{-0.05} | 46.73 ^{+0.07} _{-0.08} | 47.44 ^{+0.07} _{-0.08} | 9.99 ^{+0.88} _{-0.88} | 9.66 ^{+0.41} _{-0.41} | 0.22±1.45 | 0.46±0.72 |
| SDSSJ2310+18 ^(‡) | 6.0031 ^(†) | 8576±2362 | 5156±252 | 3224±1504 | 46.92 ^{+0.03} _{-0.04} | 46.78 ^{+0.1} _{-0.13} | 47.49 ^{+0.1} _{-0.13} | 9.55 ^{+0.32} _{-0.32} | 9.67 ^{+0.06} _{-0.08} | 0.67±0.75 | 0.51±0.15 |
| PSOJ359-06 | 6.1722 ^(†) | 3257±142 | 2653±213 | 554±39 | 46.55 ^{+0.07} _{-0.08} | 46.59 ^{+0.13} _{-0.19} | 47.3 ^{+0.13} _{-0.19} | 9.23 ^{+0.07} _{-0.09} | 9.0 ^{+0.09} _{-0.12} | 0.9±0.36 | 1.53±0.65 |
| SDSSJ0100+28 | 6.3268 ^(†) | 6647±1971 | 5742±1705 | 2496±316 | 47.58 ^{+0.01} _{-0.01} | 47.44 ^{+0.04} _{-0.04} | 48.15 ^{+0.04} _{-0.04} | 9.82 ^{+0.22} _{-0.45} | 10.1 ^{+0.2} _{-0.1} | 2.94±1.48 | 0.77±0.52 |
| ATLASJ025-33 | 6.3373 ^(†) | 6408±962 | 3302±768 | 2461±251 | 47.03 ^{+0.01} _{-0.01} | 46.95 ^{+0.02} _{-0.02} | 47.66 ^{+0.02} _{-0.02} | 9.51 ^{+0.13} _{-0.2} | 9.37 ^{+0.17} _{-0.1} | 0.88±0.73 | 0.21±0.7 |
| ULASJ0148+06 | 5.977 | 5811±368 | 4741±473 | 2906±129 | 46.85 ^{+0.01} _{-0.01} | 46.74 ^{+0.04} _{-0.04} | 47.46 ^{+0.04} _{-0.04} | 9.23 ^{+0.06} _{-0.07} | 9.58 ^{+0.08} _{-0.06} | 0.7±0.26 | 0.68±0.13 |
| PSOJ036+03 | 6.5405 ^(†) | 10131±329 | 3872±367 | 3727±135 | 46.82 ^{+0.02} _{-0.02} | 46.79 ^{+0.04} _{-0.05} | 47.5 ^{+0.04} _{-0.05} | 9.55 ^{+0.04} _{-0.05} | 9.43 ^{+0.08} _{-0.07} | 0.51±0.32 | 0.66±0.2 |
| QSOJ0439+1634 ^(c) | 6.5188 ^(†) | 5352±110 | 3329±295 | 1773±58 | 47.51 ^{+0.02} _{-0.02} | 47.62 ^{+0.03} _{-0.03} | 48.33 ^{+0.03} _{-0.03} | 9.77 ^{+0.03} _{-0.04} | 9.72 ^{+0.07} _{-0.09} | 0.63±0.3 | 1.1±0.62 |
| SDSSJ0818+17 | 5.96 | 9869±805 | 5477±334 | 3727±329 | 46.86 ^{+0.04} _{-0.04} | 46.85 ^{+0.08} _{-0.1} | 47.56 ^{+0.08} _{-0.1} | 9.55 ^{+0.1} _{-0.12} | 9.76 ^{+0.06} _{-0.07} | 0.4±0.26 | 0.6±0.13 |
| SDSSJ0836+00 | 5.773 | 6908±196 | 3793±691 | 573±77 | 47.06 ^{+0.0} _{-0.0} | 47.14 ^{+0.0} _{-0.0} | 47.85 ^{+0.0} _{-0.0} | 10.15 ^{+0.11} _{-0.14} | 9.59 ^{+0.13} _{-0.08} | 1.36±0.23 | 1.72±0.51 |
| SDSSJ0927+20 | 5.7722 ^(†) | 5480±732 | 3405±243 | 1785±166 | 46.55 ^{+0.05} _{-0.06} | 46.37 ^{+0.15} _{-0.24} | 47.08 ^{+0.15} _{-0.24} | 9.28 ^{+0.12} _{-0.18} | 9.11 ^{+0.1} _{-0.09} | 0.48±0.52 | 1.01±0.36 |
| SDSSJ1030+05 | 6.304 | 5002±391 | 3578±336 | 1092±92 | 46.64 ^{+0.05} _{-0.05} | 46.61 ^{+0.11} _{-0.14} | 47.32 ^{+0.11} _{-0.14} | 9.45 ^{+0.09} _{-0.12} | 9.27 ^{+0.09} _{-0.09} | 0.55±0.15 | 0.57±0.31 |
| SDSSJ1306+03 | 6.033 ^(†) | 4567±688 | 3825±449 | 769±189 | 46.66 ^{+0.02} _{-0.02} | 46.53 ^{+0.05} _{-0.06} | 47.24 ^{+0.05} _{-0.06} | 9.5 ^{+0.2} _{-0.37} | 9.29 ^{+0.09} _{-0.18} | 0.67±0.66 | 0.48±0.19 |
| ULASJ1319+09 | 6.1347 ^(†) | 6964±2636 | 4905±162 | 3150±2607 | 46.73 ^{+0.02} _{-0.03} | 46.58 ^{+0.07} _{-0.08} | 47.3 ^{+0.07} _{-0.08} | 9.28 ^{+0.45} _{-0.45} | 9.53 ^{+0.05} _{-0.11} | 0.71±0.49 | 0.13±0.09 |
| CFHQSJ1509-1 | 6.1225 ^(†) | 5095±828 | 3586±707 | 1021±216 | 46.59 ^{+0.03} _{-0.04} | 46.65 ^{+0.06} _{-0.08} | 47.37 ^{+0.06} _{-0.08} | 9.47 ^{+0.19} _{-0.33} | 9.3 ^{+0.15} _{-0.17} | 6.63±5.37 | 0.31±0.39 |

Notes. ^(†) Redshift from [C II] emission line (see D’Odorico et al. 2023). ^(‡) Classified as a BAL quasar (Bischetti et al. 2022). ^(a) Note: the Mg II emission line in this spectrum is very close to/within a strong telluric feature, therefore it needs to be taken with caution. ^(b) Note: the C IV emission line region in this spectrum has low S/N, therefore the derived black holes and Eddington ratios need to be taken with caution. ^(c) This quasar is gravitationally lensed (Fan et al. 2019): the values presented here are not corrected for magnification. This quasar was not included in the comparison with lower- z sources in the discussion session.

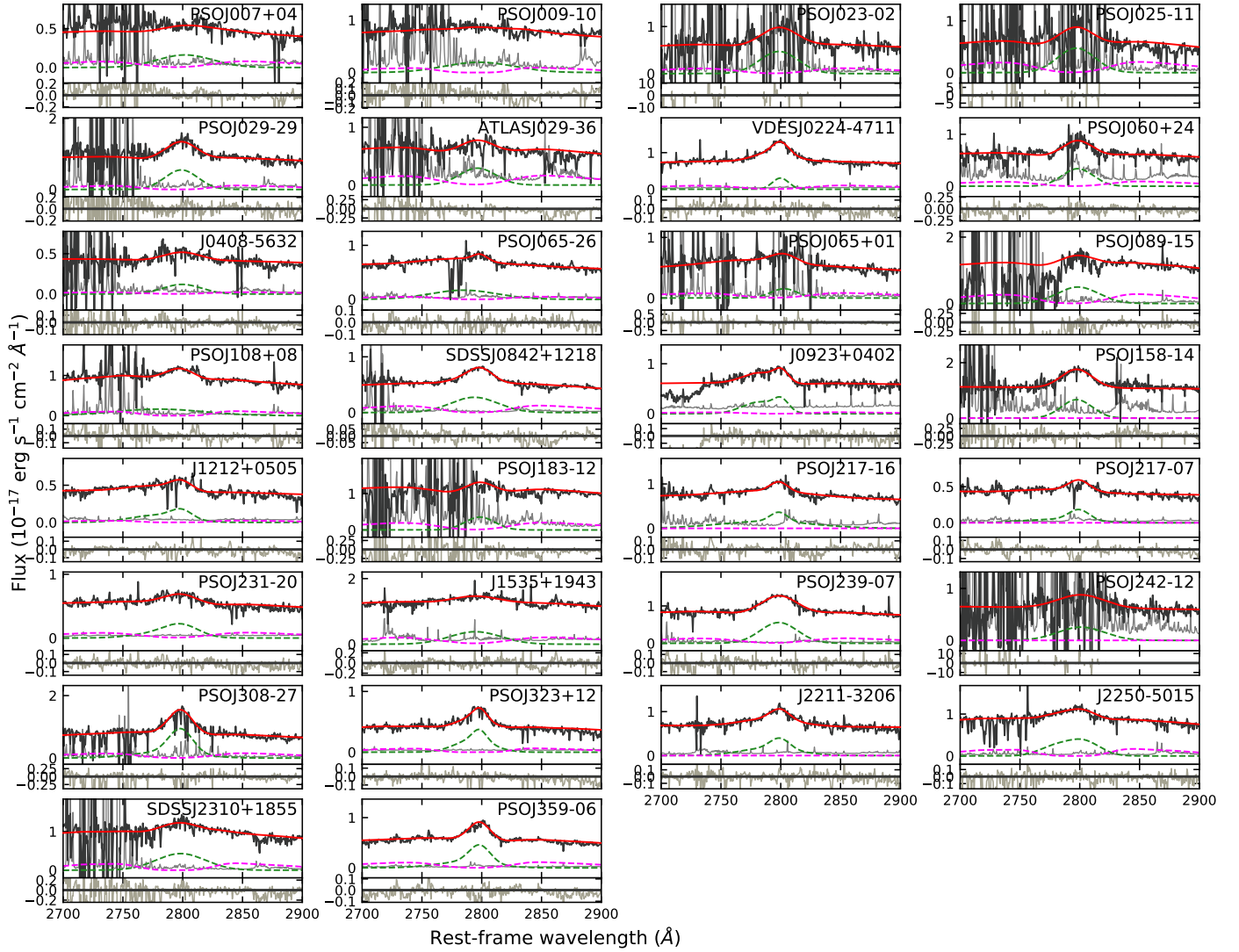


Fig. 1. Spectral region centered on the Mg II emission line for the XQR-30 sample. The pseudo-continuum (power law + Balmer contribution + Fe II empirical template) and multiple Gaussian lines fit are shown with dashed magenta and green lines, respectively, while the total fit is shown in red. We also show the residuals (in grey) in the lower panels. We note that in few cases the Mg II emission line falls partially (PSOJ007+04, PSOJ009–10, PSOJ183–12, PSOJ065+01) or fully (PSOJ023–02, PSOJ025–11, PSOJ242–12) in a region affected by telluric absorption. Despite the general high S/N of our spectra, given the (much) higher noise in these regions, the fit of these objects could be affected.

we exclude PSOJ065+01, we can obtain a mean (median) dispersion of 0.25(0.21) dex. All these values are lower than the dispersion of the CIV-based scaling relation to obtain black hole masses (see Eq. (3)), expected to be ~ 0.40 dex from the Vestergaard & Peterson (2006) relation, and are consistent with the ~ 0.24 dex scattering expected when considering the Coatman et al. (2017) correction. A larger black hole masses range would be needed to fully understand how the CIV- and Mg II-based black hole masses estimates compare.

4.3. Comparison with the literature and lower redshift samples

We place our black hole mass and Eddington ratio measurements, based on the Mg II modeling, in the context of the literature (e.g., Yang et al. 2021; Farina et al. 2022). For simplicity, in the following section, we label these quantities as M_{BH} and λ_{BH} .

To consider sources at low redshifts, we took the SDSS Data Release 7 (DR7, Richards et al. 2011) quasar catalog.

We selected objects with: (a) redshift between $0.35 < z < 2.25$, that is, with the Mg II emission line region recovered in the SDSS wavelength range; (b) valid values for $L_{\lambda}(3000)$; (c) broad Mg II emission line ($FWHM_{\text{MgII}} > 1000 \text{ km s}^{-1}$), with spectra of good quality and a reliable fit ($FWHM_{\text{MgII}} > 2 \text{ ERR}_{FWHM_{\text{MgII}}}$ and $EW_{\text{MgII}} > 2 \text{ ERR}_{EW_{\text{MgII}}}$). The sample obtained in this way is of 77 824 quasars. Regarding the high-redshift sample, we considered quasars at $z > 5.8$ with NIR spectra observed in the literature (Willott et al. 2010; De Rosa et al. 2011; Mazzucchelli et al. 2017; Chegade et al. 2018; Shen et al. 2019; Matsuoka et al. 2019; Reed et al. 2019; Onoue et al. 2019; Andika et al. 2020; Eilers et al. 2020; Schindler et al. 2020; Bañados et al. 2021; Yang et al. 2021; Farina et al. 2022; see Fan et al. 2022 for a review). We obtained 114 sources, 23 of which are also part of the E-XQR-30 sample. We report in Sect. 4.4 a comparison between the values obtained in this work and in the literature, showing an overall agreement. For the remaining part of the analysis presented below, we consider for these quasars the values of M_{BH} , L_{bol} and λ_{BH} newly

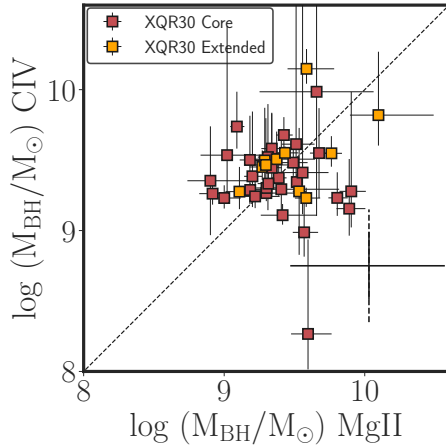


Fig. 2. Comparison between CIV- and Mg II-based black hole masses. Typical uncertainties due to the scatter in the relations used are shown with a black cross in the right-bottom corner. Uncertainties on the uncorrected Vestergaard & Peterson (2006) scaling relations (~ 0.40 dex) are shown with dashed lines.

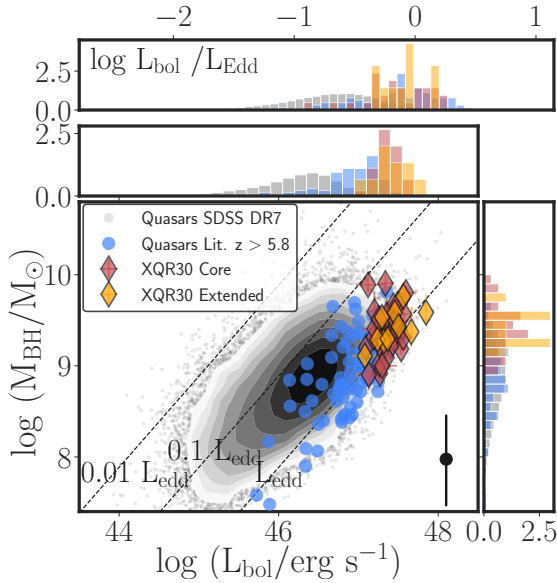


Fig. 3. Black hole masses versus bolometric luminosities. We show quasars at $0.35 < z < 2.25$ from the SDSS DR7 survey (black contours and grey points), and a sample of $z > 5.8$ quasars from the literature (blue points, see Sect. 4.3 for references). We report the newly calculated values for the core XQR-30 quasars in red diamonds, and the additional 12 high- z sources in golden diamonds. Typical systematic uncertainty on black hole masses, due to the scaling relations used (~ 0.55 dex), is shown in the bottom right corner. Distributions of bolometric luminosities, black hole masses, and Eddington ratios for all the above described samples are also reported.

derived here. In the following comparison, we excluded the quasar J0100+2802, which is a strong outlier in bolometric luminosity and does not have comparable counterparts in the SDSS survey, as well as the quasar J0439+1634, which is gravitationally lensed (Fan et al. 2019). Hence, the total sample of high-redshift quasars considered here (literature + E-XQR-30) is of 133 sources. For both the high- z quasars from the literature and the low-redshift objects from SDSS, we calculated the values of black hole masses, bolometric luminosities and Eddington ratios in a consistent way with the sample presented in this paper (see Sect. 4.1). We show in Fig. 3 the black hole masses and bolometric

metric luminosity values for the E-XQR-30 sample and for these comparison samples. As already expected from the sample selection, we see that the E-XQR-30 sample occupies the parameter space at the highest luminosities, with a mean (median) L_{bol} value of 2.3 (2.2) $\times 10^{47}$ erg s^{-1} . The mean (median) M_{BH} values are: 2.9 (2.4) $\times 10^9 M_{\odot}$ and mean (median) λ_{BH} values are: 0.84 (0.72).

In general, caution should be taken when comparing different quasars sample. First of all, it is extremely difficult to define the completeness of the high- z sample, due to the heterogeneous selection criteria of the different sub-samples (e.g., Bañados et al. 2016; Jiang et al. 2016; Matsuoka et al. 2019). This can insert systematic biases in our comparison, considering that even well defined samples can be biased (for instance a positive luminosity-dependent bias of measured black hole masses has been found; e.g. Shen & Kelly 2012; Kelly & Shen 2013; Wu et al. 2022). Secondly, we would like to highlight that, given that we derived L_{bol} using the bolometric correction from Richards et al. (2006), these values are a reflection of the quasars UV luminosities. Hence, when we match samples by bolometric luminosity distribution (see below), we are effectively considering the intrinsic UV luminosity distribution. Finally, our cut of $FWHM_{\text{MgII}} > 1000$ km s^{-1} in the low-redshift quasars selection, despite being generally considered in literature for defining broad emission lines objects (e.g., Padovani 2017), can insert a bias against slightly lower FWHM values, which in return affects BHs with lower masses. Keeping in mind these cautions, we still decide to compare the high-redshift quasars sample and the quasars at lower redshifts, in order to test for any redshift evolution in the black hole and Eddington ratio distributions.

We first considered only the sources in the E-XQR30 sample, then we utilized all high- z quasars (from this work + the literature). In order to obtain a consistent comparison, we selected a subsample of quasars from the SDSS matching the bolometric luminosity distribution of the sample of quasars at high- z . In practice, we selected sources at low- z in a range of ± 0.01 $\log L_{\text{bol}}$ for each high- z quasar, and we considered their respective M_{BH} and λ_{BH} : we repeated this trial 1000 times. The mean (median) of the black hole masses values of the low- z quasar sample matched with the E-XQR30 sources are 3.2 (2.6) $\times 10^9 M_{\odot}$. On the other hand, the mean (median) λ_{BH} values are 0.86 (0.69). We note that these values are comparable with those obtained for the E-XQR30 objects. We also performed a Kolmogorov–Smirnov (KS) test in order to assess whether the bolometric luminosity-matched low- z and E-XQR30 samples are consistent with their having been drawn from the same underlying population. We obtain a p value of $0.41/0.27$ for the $M_{\text{BH}}/\lambda_{\text{BH}}$ distribution, rejecting the hypothesis that these two samples are not drawn from the same population.

We went on to consider the entire high- z sample (this work + literature; 133 objects). In order to test how our comparison relies on the intrinsic high-redshift quasar luminosity distribution, we repeat the same comparison as above in different ranges of luminosity, following the approach from Farina et al. (2022). We consider three luminosity ranges each containing the same number of quasars: high luminosity ($\log L_{\text{bol}} > 47.17$ erg s^{-1}), medium luminosity ($46.92 < \log L_{\text{bol}} < 47.17$ erg s^{-1}), and low luminosity ($\log L_{\text{bol}} < 46.92$ erg s^{-1}). Results are reported in Fig. 4. The mean, median, and standard deviation values for L_{bol} , M_{BH} , and λ_{BH} , for the entire luminosity sample, and for each range of luminosity, for the low- and high- z samples are listed in Table 2. We repeated the KS test for this sample and for all the luminosity ranges. The resulting p -values are also reported in Table 2.

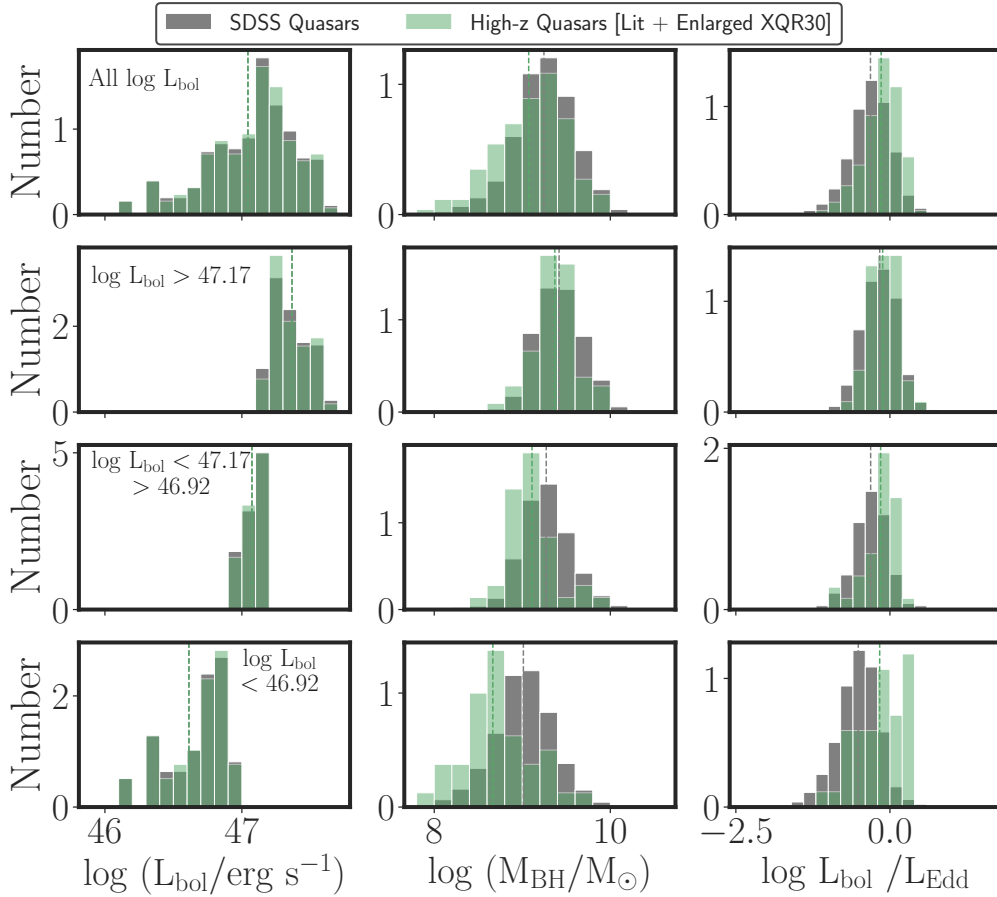


Fig. 4. Bolometric Luminosities (*left*), black hole masses (*middle*), and Eddington ratios (*right*) distributions for all the quasars at high- z (literature + enlarged XQR-30) in green, and for a bolometric luminosity matched sample at low- z . Mean values for the quantities, both at low- and high-redshift, are shown with dashed lines, in grey and green, respectively. *Top row*: all the luminosity distribution of high- z quasars. The *second* to the *last rows*: samples divided by luminosity ranges, each containing the same number of high- z quasars, from high to medium to low luminosities. See Sect. 4.3 for further details on the samples compilation and matching. The Eddington ratio distribution at high- z is shifted to marginally higher values than at lower z , for the entire luminosity case and for each luminosity range. We note that with decreasing luminosity, the separation between the high- and low-redshift sample is increasing, albeit with larger dispersions.

We note that the bolometric luminosity distribution in the low- z sample is constructed to be consistent with that at high- z . This is also reflected in the corresponding p -values of 1 for all the cases (see Table 2). We find that the mean and median black hole mass/Eddington ratio values are lower/higher in the high-redshift sample with respect to the low- z one, considering all luminosities, and in every luminosity range. However, we note that these differences with redshifts are more significant at lower luminosities, with a difference between the mean Eddington ratio at high- and low- z of ~ 0.38 in the low luminosity range, namely, it is higher with respect to what is observed for luminous objects (~ 0.03). We can also notice that the distributions of M_{BH} and λ_{BH} have slightly larger dispersions at lower luminosities. For instance, the standard deviation for the high- z black hole masses (Eddington ratios) is 0.45(0.38)dex in the low luminosity range, with respect to a standard deviation of 0.25(0.24)dex in the high luminosity range. These trends can also be reflected in the results of the KS test. Indeed, in the high luminosity range, the p -values obtained by comparing the black hole masses and Eddington ratios distributions at high- and low- z are relatively high (0.47 and 0.32, respectively). Conversely, in the medium and low luminosity ranges, and when considering all luminosities, we recovered low p -values ($< 10^{-4}$), reject-

ing the hypothesis that these quantities are drawn from the same underlying distribution.

In summary, our analysis suggests that quasars at high redshift accrete slightly faster than those in a bolometric luminosity distribution matched sample at $z \sim 1.5$, assuming the same mean radiative efficiency. This trend increases for the faintest objects discovered, albeit with a larger dispersion. In other words, at high-redshift, we observe that the most luminous quasars are powered by less massive SMBHs, accreting at slightly higher rates compared to a luminosity-matched sample at high- z . This result is in contrast with respect to previous works (e.g., Mazzucchelli et al. 2017; Shen et al. 2019), which did not recover a change in the mean Eddington ratio value with z , and with expectations from the consistency between composite spectra of quasars at $z \gtrsim 6$ and at lower- z (e.g., Shen et al. 2019; Yang et al. 2021). On the other hand, our outcome is in agreement with the recent results by Yang et al. (2021) and Farina et al. (2022), where a similar increase was observed in the mean value of the Eddington ratio as that measured in this work. Also, we may notice that the composite spectra obtained in the literature are usually focused on the higher luminosity quasars, both at high- and low- z (e.g., Vanden Berk et al. 2001; Selsing et al. 2016), where the changes between the two samples are less apparent (see Fig. 4 and Table 2).

Table 2. Mean, median, and standard deviation of bolometric luminosities, black hole masses, and Eddington ratios distribution shown in Fig. 4, for the low- and high- z quasars samples.

| | High- z quasars | | | Low- z quasars | | | KS-test |
|---|-------------------|--------|---------|------------------|--------|---------|--------------------|
| | Mean | Median | St. Dev | Mean | Median | St. Dev | p -value |
| All luminosity | | | | | | | |
| L_{bol} [10^{47} erg s $^{-1}$] | 1.49 | 1.32 | 0.38 | 1.49 | 1.32 | 0.38 | 1 |
| M_{BH} [$10^9 M_{\odot}$] | 1.79 | 1.40 | 0.45 | 2.44 | 1.80 | 0.35 | 2×10^{-4} |
| λ_{BH} | 0.89 | 0.76 | 0.30 | 0.62 | 0.50 | 0.34 | 2×10^{-8} |
| High luminosity: $L_{\text{bol}} > 10^{47.17}$ erg s $^{-1}$ | | | | | | | |
| L_{bol} [10^{47} erg s $^{-1}$] | 2.47 | 2.18 | 0.14 | 2.47 | 2.17 | 0.14 | 1.0 |
| M_{BH} [$10^9 M_{\odot}$] | 2.74 | 2.18 | 0.25 | 3.19 | 2.53 | 0.28 | 0.47 |
| λ_{BH} | 0.88 | 0.73 | 0.24 | 0.85 | 0.69 | 0.28 | 0.32 |
| Medium luminosity: $10^{46.92} < L_{\text{bol}} < 10^{47.17}$ erg s $^{-1}$ | | | | | | | |
| L_{bol} [10^{47} erg s $^{-1}$] | 1.20 | 1.26 | 0.07 | 1.20 | 1.26 | 0.07 | 1.0 |
| M_{BH} [$10^9 M_{\odot}$] | 1.61 | 1.28 | 0.27 | 2.38 | 1.81 | 0.30 | 1×10^{-4} |
| λ_{BH} | 0.84 | 0.76 | 0.28 | 0.61 | 0.51 | 0.29 | 6×10^{-5} |
| Low luminosity: $L_{\text{bol}} < 10^{46.92}$ erg s $^{-1}$ | | | | | | | |
| L_{bol} [10^{47} erg s $^{-1}$] | 0.49 | 0.58 | 0.30 | 0.49 | 0.58 | 0.30 | 1.0 |
| M_{BH} [$10^9 M_{\odot}$] | 0.52 | 0.52 | 0.45 | 1.46 | 1.03 | 0.35 | 10^{-8} |
| λ_{BH} | 0.79 | 0.77 | 0.38 | 0.41 | 0.32 | 0.34 | 3×10^{-9} |

Notes. We also report the p -values obtained with a Kolmogorov–Smirnov test.

4.4. Comparison between XQR-30 and literature values

We note that 23 objects reported in the E-XQR-30 sample already have observations reported in the literature. In case of sources observed by more than one study, we considered only the most recent measurement: J0142–3327 (Chehade et al. 2018); PSO060+24 (Shen et al. 2019); J0224–4711 (Reed et al. 2019); J0923+0402, J1535+1943 (Yang et al. 2021); PSO239–07, J2211–3206, J0842+1218, PSO231–20, PSO158–14, PSO007+04, PSO065–26, PSO183+05, J2310+1855, PSOJ359–06, PSOJ323+12, J1319+0950, PSO036+03, J1030+0524, J1306+0356, J1509–1749, and J0100+2802 (Farina et al. 2022). The quasar J0439+1634 was also observed by Yang et al. (2021), but given that this source is lensed (Fan et al. 2019), we decided to not include it in this comparison. We show in Fig. 5 the comparison of the bolometric luminosities, black hole masses, and Eddington ratios (from the Mg II emission line model), all calculated with a consistent method (see Sect. 4.1). In general, we note that there are no recovered systemic trends between the quantities derived here and those from the literature. The major outlier reported here is PSOJ007+04, whose Mg II emission line was fitted in this work with a very broad Gaussian (see Table 1 and Fig. 1). This resulted in a very large black hole mass and a low Eddington ratio, which stands in contrast to what is presented in Farina et al. (2022). This is due to the fact that the Mg II line in this quasar is very close to a telluric absorption, hence, its modeling should be approached with caution (see Fig. 1 and Table 1).

5. Conclusions

The E-XQR-30 sample provides us with a unique opportunity to study quasars at high- z with spectra of exquisite quality and high S/N. Here, we calculated their bolometric luminosities via the monochromatic luminosity at rest frame 3000 Å. We obtained the black hole mass values by modeling the C IV and Mg II emission

line regions, using scaling relation calibrated in the local universe (Vestergaard & Peterson 2006; Vestergaard & Osmer 2009). In particular, we accounted for the non-virial component of the C IV emission line, due to outflows or wings, utilizing the correction from Coatman et al. (2017). We observe that in our sample, the black hole mass values obtained with the two emission lines cover the same parameter space (see Fig. 2). Assuming that the Mg II-based estimates are the more reliable, the scatter of the C IV-based measurements is lower than that measured around the Vestergaard & Peterson (2006) scaling relation (~ 0.4 dex), and it is consistent or slightly greater than what is expected after the Coatman et al. (2017) correction (~ 0.24 dex).

We compared the values measured from the E-XQR-30 objects with those of other quasars at $z > 5.8$ obtained from the literature, and from a sample of quasars at $0.35 < z < 2.25$ from the SDSS DR7 survey (see Fig. 3). We considered a comparison sub-sample of quasars at low- z , matched to the entire high- z quasars' bolometric luminosity distribution. The high-redshift Eddington ratio distribution is slightly higher with respect to the matched low- z sample (i.e., with a difference between the mean λ_{BH} values of ~ 0.27 ; see Fig. 4 and Table 2). We repeated this comparison considering sub-samples of high- and low- z quasars in different bolometric luminosity ranges, noting that this increase in the mean Eddington ratio at higher redshifts is present in every luminosity range and is more apparent at lower luminosities. This suggests that quasars at $z \gtrsim 6$ accrete marginally faster than at $z \sim 1$, as suggested in other recent works in the literature (e.g., Yang et al. 2021; Farina et al. 2022).

In the future, it will be crucial to explore the properties of quasars over larger ranges of luminosity and black hole masses, thanks to the discoveries that will be enabled by future surveys as well, such as the Legacy Survey of Space and Time (LSST) at Vera Rubin Observatory (e.g., Ivezić et al. 2014, 2019) and the Euclid survey (e.g., Euclid Collaboration 2019). On the other hand, it will also be important to measure black hole masses

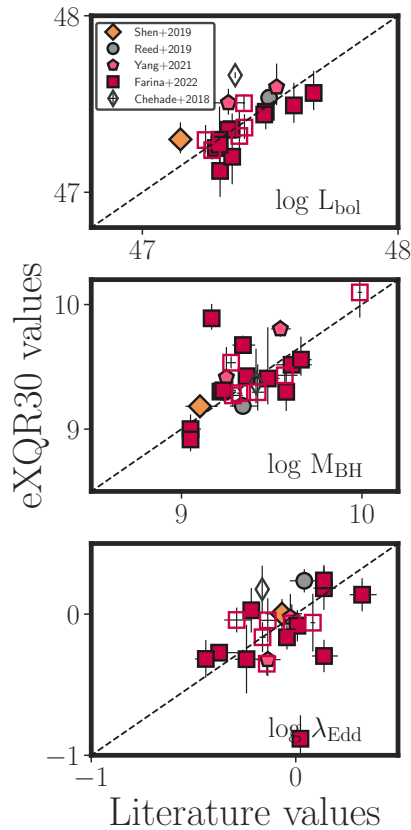


Fig. 5. Comparison between bolometric luminosities (*upper*), black hole masses (*central*), and Eddington ratios (*lower panel*) for the quasars in the enlarged XQR-30 sample that were previously observed and studied in the literature: black diamond (Chehade et al. 2018), yellow diamond (Shen et al. 2019), grey circle (Reed et al. 2019), pink pentagon (Yang et al. 2021), and red squares (Farina et al. 2022). The dashed black line denotes the one-to-one relation. The filled symbols represent data of sources from the core XQR-30 survey, while empty ones show data from the literature sample.

from other emission lines, such as $H\beta$, which are directly related to the reverberation mapping studies at low- z , and to test whether there are any systematic difference with values obtained from the C IV or Mg II line modeling (e.g., Homayouni et al. 2020). The *James Webb Telescope* will play a key role in pursuing such studies (e.g., Eilers et al. 2023; Larson et al. 2023; Yang et al. 2023; Maiolino et al. 2023).

Acknowledgements. G.B. was supported by the National Science Foundation through grant AST-1751404. E.P.F. is supported by the international Gemini Observatory, a program of NSF's NOIRLab, which is managed by the Association of Universities for Research in Astronomy (AURA) under a cooperative agreement with the National Science Foundation, on behalf of the Gemini partnership of Argentina, Brazil, Canada, Chile, the Republic of Korea, and the United States of America. R.A.M. acknowledge support from the ERC Advanced Grant 740246 (Cosmic_Gas). S.C. is supported by European Union's HE ERC Starting Grant No. 101040227 – WINGS. This work is based on observations collected at the European Southern Observatory under ESO large program 1103.A-0817(A).

References

Andika, I. T., Jahnke, K., Onoue, M., et al. 2020, *ApJ*, 903, 34
 Bañados, E., Venemans, B. P., Decarli, R., et al. 2016, *ApJS*, 227, 11
 Bañados, E., Venemans, B. P., Mazzucchelli, C., et al. 2018, *Nature*, 553, 473
 Bañados, E., Mazzucchelli, C., Momjian, E., et al. 2021, *ApJ*, 909, 80
 Becker, G. D., Bolton, J. S., Madau, P., et al. 2015, *MNRAS*, 447, 3402

Becker, G. D., Pettini, M., Rafelski, M., et al. 2019, *ApJ*, 883, 163
 Begelman, M. C., Volonteri, M., & Rees, M. J. 2006, *MNRAS*, 370, 289
 Bischetti, M., Feruglio, C., D'Odorico, V., et al. 2022, *Nature*, 605, 244
 Bond, J. R., Arnett, W. D., & Carr, B. J. 1984, *ApJ*, 280, 825
 Bosman, S. E. I., Fan, X., Jiang, L., et al. 2018, *MNRAS*, 479, 1055
 Chehade, B., Carnall, A. C., Shanks, T., et al. 2018, *MNRAS*, 478, 1649
 Coatman, L., Hewett, P. C., Banerji, M., et al. 2017, *MNRAS*, 465, 2120
 Cupani, G., Calderone, G., Cristiani, S., et al. 2018, *SPIE Conf. Ser.*, 10707, 1070723
 Cupani, G., D'Odorico, V., Cristiani, S., et al. 2020, *SPIE Conf. Ser.*, 11452, 114521U
 Davies, F. B., Hennawi, J. F., & Eilers, A.-C. 2019, *ApJ*, 884, L19
 De Rosa, G., Decarli, R., Walter, F., et al. 2011, *ApJ*, 739, 56
 De Rosa, G., Venemans, B. P., Decarli, R., et al. 2014, *ApJ*, 790, 145
 Denney, K. D., Horne, K., Shen, Y., et al. 2016, *ApJS*, 224, 14
 Devecchi, B., & Volonteri, M. 2009, *ApJ*, 694, 302
 Dietrich, M., Hamann, F., Appenzeller, I., & Vestergaard, M. 2003, *ApJ*, 596, 817
 D'Odorico, V., Bañados, E., Becker, G. D., et al. 2023, *MNRAS*, 523, 1399
 Eilers, A.-C., Hennawi, J. F., Decarli, R., et al. 2020, *ApJ*, 900, 37
 Eilers, A.-C., Simcoe, R. A., Yue, M., et al. 2023, *ApJ*, 950, 68
 Euclid Collaboration (Barnett, R., et al.) 2019, *A&A*, 631, A85
 Fan, X., Wang, F., Yang, J., et al. 2019, *ApJ*, 870, L11
 Fan, X., Bañados, E., & Simcoe, R. A. 2022, ArXiv e-prints [arXiv:2212.06907]
 Farina, E. P., Schindler, J.-T., Walter, F., et al. 2022, *ApJ*, 941, 106
 Ferrara, A., Salvadori, S., Yue, B., & Schleicher, D. 2014, *MNRAS*, 443, 2410
 Homayouni, Y., Trump, J. R., Grier, C. J., et al. 2020, *ApJ*, 901, 55
 Inayoshi, K., Visbal, E., & Haiman, Z. 2020, *ARA&A*, 58, 27
 Ivezić, Ž., Brandt, W. N., Fan, X., et al. 2014, in *Multiwavelength AGN Surveys and Studies*, eds. A. M. Mickaelian, & D. B. Sanders, 304, 11
 Ivezić, Ž., Kahn, S. M., Tyson, J. A., et al. 2019, *ApJ*, 873, 111
 Jiang, L., Fan, X., Ivezić, Ž., et al. 2007, *ApJ*, 656, 680
 Jiang, L., McGreer, I. D., Fan, X., et al. 2015, *AJ*, 149, 188
 Jiang, L., McGreer, I. D., Fan, X., et al. 2016, *ApJ*, 833, 222
 Jones, A., Noll, S., Kausch, W., Szyszka, C., & Kimeswenger, S. 2013, *A&A*, 560, A91
 Kelly, B. C., & Shen, Y. 2013, *ApJ*, 764, 45
 Kurk, J. D., Walter, F., Fan, X., et al. 2007, *ApJ*, 669, 32
 Lai, S., Bian, F., Onken, C. A., et al. 2022, *MNRAS*, 513, 1801
 Larson, R. L., Finkelstein, S. L., Kocevski, D. D., et al. 2023, *ApJ*, submitted [arXiv:2303.08918]
 López, S., D'Odorico, V., Ellison, S. L., et al. 2016, *A&A*, 594, A91
 Maiolino, R., Scholtz, J., Witstok, J., et al. 2023, ArXiv e-prints [arXiv:2305.12492]
 Matsuoka, Y., Onoue, M., Kashikawa, N., et al. 2019, *ApJ*, 872, L2
 Mazzucchelli, C., Bañados, E., Venemans, B. P., et al. 2017, *ApJ*, 849, 91
 Meyer, R. A., Bosman, S. E. I., & Ellis, R. S. 2019, *MNRAS*, 487, 3305
 Neeleman, M., Novak, M., Venemans, B. P., et al. 2021, *ApJ*, 911, 141
 Noll, S., Kausch, W., Barden, M., et al. 2012, *A&A*, 543, A92
 Oh, S. P., & Haiman, Z. 2002, *ApJ*, 569, 558
 Onoue, M., Kashikawa, N., Matsuoka, Y., et al. 2019, *ApJ*, 880, 77
 Padovani, P. 2017, *Nat. Astron.*, 1, 0194
 Pensabene, A., Carniani, S., Perna, M., et al. 2020, *A&A*, 637, A84
 Reed, S. L., Banerji, M., Becker, G. D., et al. 2019, *MNRAS*, 487, 1874
 Richards, G. T., Haiman, Z., Pindor, B., et al. 2006, *AJ*, 131, 49
 Richards, G. T., Kruczek, N. E., Gallagher, S. C., et al. 2011, *AJ*, 141, 167
 Sakurai, Y., Yoshida, N., Fujii, M. S., & Hirano, S. 2017, *MNRAS*, 472, 1677
 Schindler, J.-T., Farina, E. P., Bañados, E., et al. 2020, *ApJ*, 905, 51
 Selsing, J., Fynbo, J. P. U., Christensen, L., & Krogager, J.-K. 2016, *A&A*, 585, A87
 Shen, Y., & Kelly, B. C. 2012, *ApJ*, 746, 169
 Shen, Y., Wu, J., Jiang, L., et al. 2019, *ApJ*, 873, 35
 Trakhtenbrot, B., & Netzer, H. 2012, *MNRAS*, 427, 3081
 Valiante, R., Schneider, R., Volonteri, M., & Omukai, K. 2016, *MNRAS*, 457, 3356
 Vanden Berk, D. E., Richards, G. T., Bauer, A., et al. 2001, *AJ*, 122, 549
 Vernet, J., Dekker, H., D'Odorico, S., et al. 2011, *A&A*, 536, A105
 Vestergaard, M., & Osmer, P. S. 2009, *ApJ*, 699, 800
 Vestergaard, M., & Peterson, B. M. 2006, *ApJ*, 641, 689
 Vestergaard, M., & Wilkes, B. J. 2001, *ApJS*, 134, 1
 Volonteri, M. 2010, *A&ARv*, 18, 279
 Volonteri, M., Habouzit, M., & Colpi, M. 2021, *Nat. Rev. Phys.*, 3, 732
 Wang, F., Yang, J., Fan, X., et al. 2021, *ApJ*, 907, L1
 Willott, C. J., Delorme, P., Reylé, C., et al. 2010, *AJ*, 139, 906
 Wu, J., Shen, Y., Jiang, L., et al. 2022, *MNRAS*, 517, 2659
 Yang, J., Wang, F., Fan, X., et al. 2020, *ApJ*, 897, L14
 Yang, J., Wang, F., Fan, X., et al. 2021, *ApJ*, 923, 262
 Yang, J., Wang, F., Fan, X., et al. 2023, *ApJ*, 951, L5